Comparison of simulated scattering characteristics of large rain drops and a special form of melting hail and relation to C, S and X band radar observations

S. Manic, E. Chobanyan, M. Thurai, V. N. Bringi, and B. M. Notaroš
[1]Colorado State Univ., Fort Collins, CO

1. Introduction

Rain drops and melting hail differ not only in their shapes and sizes but also in terms of their dielectric properties. These differences in physical properties between rain and wet hail result in differing scattering and propagation characteristics depending on radar frequency. For example in several early measurements of Z_{dr} at C-band at times exceeding 7-8 dB were ascribed to resonant scattering by melting hail (Meischner et al. 1991). Further, Tabary et al. (2009) deduced exceedingly large values of differential attenuation between H and V polarizations at C-band and ascribed this to a melting model of hail where a torus of melt water forms around the equator leading to stable fall mode (Rasmussen and Heymsfield, 1987). Scattering from such complex two-layer shapes have not been modelled yet and is the focus of this paper. Our interest is not only in differential attenuation but also Z_{dr} differences at S, C and X-bands. One application is to dual-wavelength (S/X-bands) and dual-polarized radar (CSU-CHILL) measurements in intense convection whereby direct measurements of both absolute and differential attenuation are possible (CSU_CHILL, 2015, see http://www.chill.colostate.edu/ and click under articles, 2015).

Simulations are carried out at C band as well as S and X bands. For C-band, results of specific differential attenuation, differential phase, and differential reflectivity for such hydrometeors have already been published (Thurai et al., 2015). We present the corresponding results for S and X bands, and additionally discuss CSU-CHILL S and X band radar observations during a rain with small melting hail mixed event.

2. Hydrometeor shapes/dimensions

2.1 Rain drops

Based on thousands of 2D-video disdrometer measurements of large raindrops, the most probable shape (taking into account drop oscillations) has been shown to be a ‘smoothed' conical shape that can be described by a closed-form empirical formula in the Cartesian coordinates, the parameters of which depends only on the equi-volumetric sphere diameter, D_{eq}. The set of equations can be found in Thurai et al., (2007). Fig. 1 shows a three-dimensional (3D) shape of a 7 mm drop along with the projection onto the x-z and y-z planes. Since these raindrop shapes are smooth and rotationally symmetric, their polarimetric radar parameters are calculated using the fast T-matrix code.

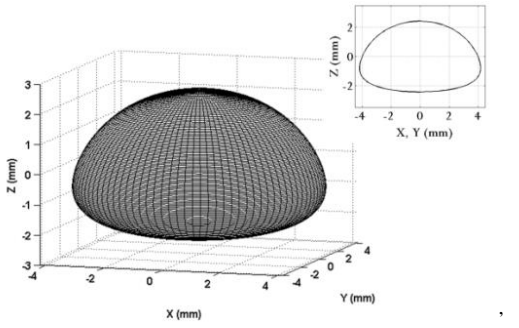

Fig. 1: 3D shape of a 7 mm D_{eq} rain drop, and the projections on to x-z and y-z plane.

2.2 Melting hail

For the special form of melting hail, we model the hydrometeor as an ice-sphere in the center, surrounded by a water torus, with also a thin layer of water over the top and bottom of the ice sphere. Two 'shapes' are considered: (i) based on the aircraft probe image given in Fig. 7.46 of Bringi and Chandrasekar (2001), and (ii) based on the 2DVD image obtained during a rain-hail event which occurred in Greeley Colorado on 5 July 2015. These are shown in Fig. 2. The top panel shows a depiction of the first model and the second panel shows the aircraft probe image. The third panel shows the depiction of the second model and the fourth panel shows the 2DVD based image.

3. EM scattering modelling

To perform scattering simulations, we first consider an arbitrarily shaped particle model situated in free space excited by a time-harmonic electro-magnetic field of angular frequency, ω. The particle can consist of an arbitrary number of parts with different dielectrics with different permittivity,ε, and different permeability, μ. According to the surface equivalence principle the entire system is divided into subsystems (domains): interior subsystems modeling different dielectric domains in the particle and one exterior subsystem with air as dielectric. Subsystems are separated by equivalent surfaces, one placed on the interface of each dielectric domain. The equivalent surface represents one of the dielectric regions (domains), with the remaining space being filled with the same medium. The equivalent surface electric ($\mathbf{J_s}$) and magnetic ($\mathbf{M_s}$) currents are placed on the boundary surface of each domain such that they produce zero total field in the space outside that domain. The boundary conditions for the tangential components of the total electric and magnetic field vectors on the boundary surface between any two adjacent dielectric domains yield:

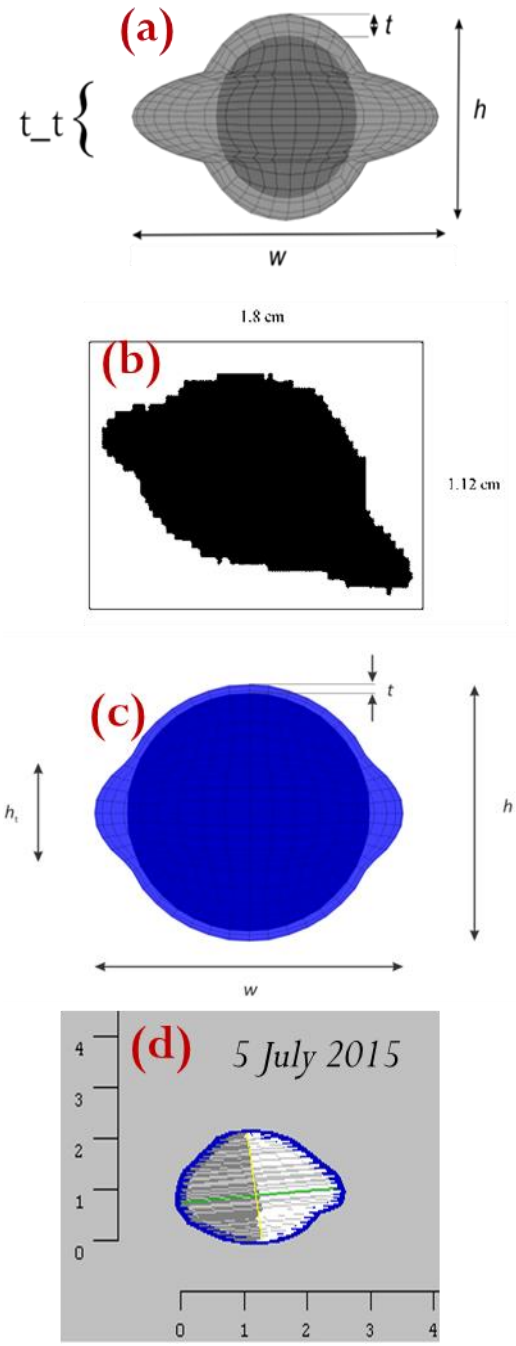

Fig. 2: (a) Depiction of model (A) with spherical ice-core, and water torus surrounding it; (b) dimensions used for model (A) (see text); (c) depiction of model (B); (d) 2DVD based image (in mm) used for dimensioning model (B).

$$[\mathbf{E}(\mathbf{J}_s,\mathbf{M}_s,\varepsilon_j,\mu_j)]_{tang}+(\mathbf{E}_i)_{tang}=[\mathbf{E}(-\mathbf{J}_s,-\mathbf{M}_s,\varepsilon_k,\mu_k)]_{tang} \quad \ldots\ldots\ldots\ldots (1)$$

$$[\mathbf{H}(\mathbf{J}_s,\mathbf{M}_s,\varepsilon_j,\mu_j)]_{tang}+(\mathbf{H}_i)_{tang}=[\mathbf{H}(-\mathbf{J}_s,-\mathbf{M}_s,\varepsilon_k,\mu_k)]_{tang} \quad \ldots\ldots\ldots\ldots (2)$$

where ε_j and μ_j are permittivity and permeability of the j-th domain, $\mathbf{E}(\mathbf{J}_s,\mathbf{M}_S,\varepsilon,\mu)$ and $\mathbf{H}(\mathbf{J}_s,\mathbf{M}_S,\varepsilon,\mu)$ are the scattered electric and magnetic fields in the region of complex permittivity ε and complex permeability μ, $\mathbf{E_i}$ and H_i are complex field-intensities of the incident wave that are non-zero just in the exterior domain in the case of particle scattering. By representing scattered fields in equations (1) and (2) in terms of vector and scalar potentials, we obtain system of equations, with $\mathbf{J_s}$ and $\mathbf{M_s}$ as unknowns. Details can be found in Djordjevic and Notaros, (2004). The system is discretized with method of moments (MoM) technique using Lagrange-type curved parametric quadrilaterals of arbitrary geometrical orders K_u, and K_v, (K_u, $K_v \geq 1$), determined by $M=(K_u + 1)(K_v + 1)$ interpolation nodes arbitrarily positioned in space shown in Fig. 3 and analytically described in Djordjevic and Notaros, (2004).

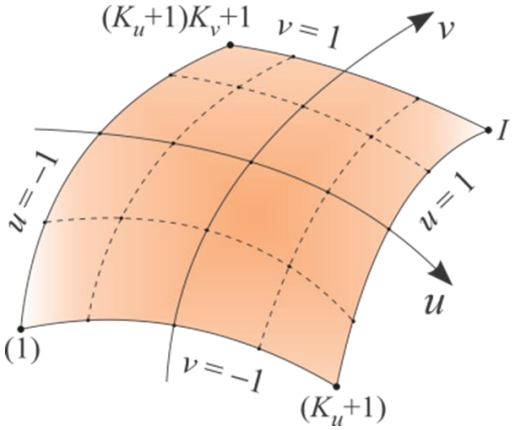

Fig. 3 Generalized curved parametric quadrilateral SIE element of geometrical orders K_u and K_v (K_u, $K_v \geq 1$), determined by $N = (K_u + 1)(K_v + 1)$ interpolation nodes arbitrarily positioned in space.

The surface electric and magnetic current densities ($\mathbf{J}_s$ and $\mathbf{M}_s$) over curvilinear quadrilaterals are expanded in terms of 2-D hierarchical divergence-conforming polynomial functions as follows

$$\mathbf{J}_s(u,v)=\sum_{i=0}^{N_u}\sum_{j=0}^{N_v-1}\alpha_{uij}\,\mathbf{f}_{uij}+\sum_{i=0}^{N_u-1}\sum_{j=0}^{N_v}\alpha_{vij}\,\mathbf{f}_{vij} \quad (3)$$

$$\mathbf{M}_S(u,v)=\sum_{i=0}^{N_u}\sum_{j=0}^{N_v-1}\beta_{uij}\,\mathbf{f}_{uij}+\sum_{i=0}^{N_u-1}\sum_{j=0}^{N_v}\beta_{vij}\,\mathbf{f}_{vij} \quad (4)$$

where vector basis functions $\mathbf{f}_{uij}$ and $\mathbf{f}_{vij}$ are defined in Djordjevic and Notaros, (2004), N_u and N_v are the adopted degrees of the polynomial current approximation, and α_{uij}, α_{vij}, β_{uij} and β_{vij} are unknown current-distribution expansion coefficients. In order to generate the system of linear equations with {α} in (3) and {β} in (4) as unknowns, equations (1) and (2) are tested by means of the Galerkin method. The system of linear equations so derived, represented in a matrix form, is solved by a direct matrix solver, based on LU-factorization.

Also, as an example, the melting hail model shown in Fig. 2(c) contains 1360 1st order quadrilateral elements. The spherical surface between ice and water is modeled by 600 elements while the outer boundary surface between water and air is modeled by 760 elements.

4. Previous results at C-band

As mentioned earlier, the C-band simulation results have been published recently (Thurai et al., 2015). The simulations were made for hydrometeors based on model (A). For such a case, *w* in Fig. 2(a) was initially set to 16.8 mm, *h* to 9.7 mm and *t* to

0.4 mm; then these values were scaled. from 50 – 150 % of the original value.

The A_{dp} factor, given by $Im\{f_{hh}-f_{vv}\}$, calculated for rain drops and melting hail are shown in Fig. 3. Here *f* is the forward scattering amplitude for *h* (horizontal) and *v* (vertical) polarizations, and the A_{dp} factor is directly related to specific differential attenuation. For both types of hydrometeors, the x-axis represents the maximum horizontal dimension. For rain, the corresponding range of D_{eq} considered is 1.5 mm to 9 mm. For the hail particles, the dimensions in Fig. 2 are varied from 50% to 150% of the original value. This applies to not just for *w* but also for the corresponding *h* and *t*.

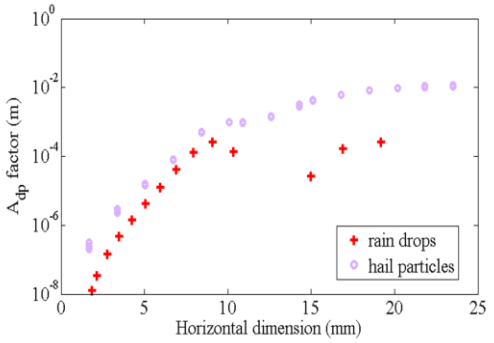

Fig. 4: C-band A_{dp} factor calculated for rain drops (red) and melting hail (purple). T-matrix method [Mishchenko et al., 1996] is used for rain drops and MoM-SIE technique is used for melting hail. For explanation of the x-axis, see text.

The resonance region for rain can be seen at around D_{eq} of 6−8 mm (i.e., horizontal dimensions of ~10−15 mm). This is to be expected at C-band. Also seen is that the A_{dp} factor values are generally larger for hail particles compared with rain drops, which could explain the higher differential attenuation reported in previous studies at C-band. Other C-band results can be seen in Thurai et al. (2015).

5. Z_{dr} for S band

Our calculations are currently being extended to S and X frequency bands. In particular, we have been focusing on single particle Z_{dr}. Both models given in Fig. 2 are considered. For model A, the same dimensions are used as before. For model B, the dimensions were estimated from the image given in the fourth panel of Fig. 2:

h = 2.12 mm, *w = 2.5 mm,*
t_t = 0.85 mm, *t = 0.08 mm*

The upper limit of *w* was set at 20 mm since such hydrometeors are not thought to exist beyond it.

The S-band simulation results are given in Fig. 5(a) in terms of Z_{dr} calculated from the back scatter amplitudes for *h* and *v* polarizations. Results using the MoM-SIE as well as those using the commercial codes HFSS-FEM (finite element method) and HFSS-IE are included, all using the same symbols, colors etc. The HFSS-FEM results were sometimes inconsistent with the other two and can be seen as outliers.

In general, we see that the computed Z_{dr} values are very sensitive to the model used. The two models can be considered as the upper and lower limits for such hydrometeors, hence we would expect Z_{dr} values to lie somewhere in-between. The calculated Z_{dr} values are much larger than those for rain (shown in Fig. 5) for the smaller particle sizes whereas for larger particle sizes, the reverse appears to be the case. The particle image shown in Fig. 2(d) can be considered to be a small particle with a horizontal dimension *w* = 2.5 mm, and from Fig. 5 one would expect its Z_{dr} to lie between 1.9 dB and 7.5 dB depending on the 'shape' of the ice-sphere – water torus scatterer. This range of values is larger than those expected for equi-

volume rain drops (D_{eq} = 2.4 mm) which is around 1 dB.

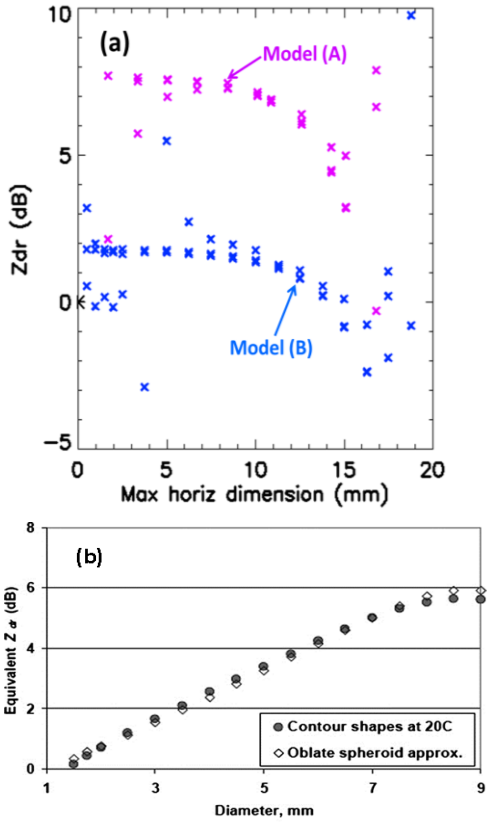

Fig. 5: Calculated S-band Z_{dr} for (a) model (A) (purple) and model (B) (blue) of melting hail, and (b) rain drops. For rain, x-axis is D_{eq}.

CHILL radar observations made during this event showed regions of moderate reflectivity (Z_h) but with relatively high differential reflectivity. Fig. 6 shows the Z_h and Z_{dr} sector scans performed at 02:39 UTC. The white circled area shows this region. Our instrumented site lies within this area (13 km from the radar, along an azimuth of 170.85 deg). The 2DVD image shown in Fig. 2(d) was recorded at 02:40 UTC. Hence it is very likely that moderate Z_h and relatively high Z_{dr} indicates the presence of these hydrometeors. By contrast the yellow-circled regions in Fig. 5 showing moderate Z_h and low Z_{dr} are likely to be predominantly rain regions, and very probably with small and moderate sized drops. The Z_{dr} calculations shown in Fig. 5 corroborate these notions.

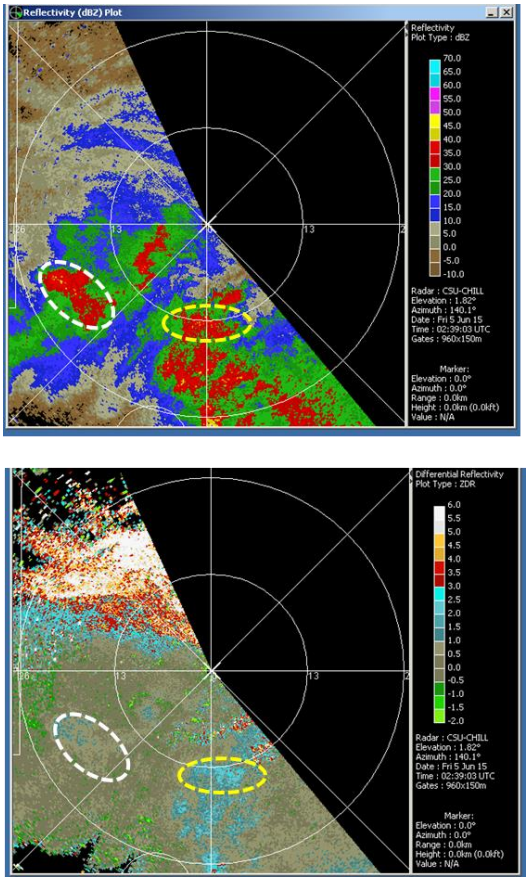

Fig. 6: CSU_CHILL S-band PPI scan on 05 June 2015, 02:39 UTC. Yellow-circled regions show moderate Z_h and low Z_{dr} (expected for rain) whereas white circled regions show moderate Z_h but relatively high Z_{dr} (consistent with results for our hail particles).

6. X-band Z_{dr}

Our X-band calculations showed more variation of Z_{dr} with the maximum horizontal dimension of the melting hail, at least for model (A). Fig. 7 shows the calculated Z_{dr} at X-band, once again for (a) hail particles and (b) rain drops. Whereas for rain drops, Z_{dr} generally increases with drop dimension (except for D_{eq} at around 4 mm), model (A) of the melting hydrometeor shows a fast

decrease with maximum horizontal dimension beyond 10 mm, and in fact becomes very negative beyond 15 mm. Model (B) shows more stable Z_{dr} variation with horizontal dimension for smaller sizes but they also become very negative for the larger sizes.

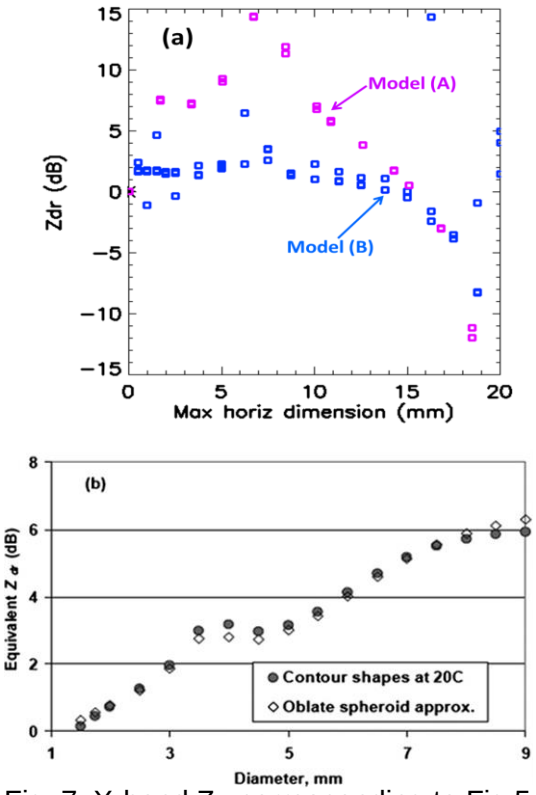

Fig. 7: X-band Z_{dr} corresponding to Fig 5

Our scattering calculations have shown that S band Z_{dr} can be substantially different from X band Z_{dr}, especially for the larger particles for which X-band Z_{dr} becomes very negative. Fig. 8 shows CHILL S and X band RHI scans taken during a convective storm. The X-band Z_{dr} panel (third panel) shows an abrupt change at around 30 km range reducing from 2.5-3 dB to less than -3 dB within about a km. Such abrupt reduction cannot be explained by differential attenuation; it is very probably due to scattering. In the same region, the S-band Z_{dr} is around 0 dB. Such features are consistent with our calculations for the larger sized hydrometeors (i.e. 15 mm or higher).

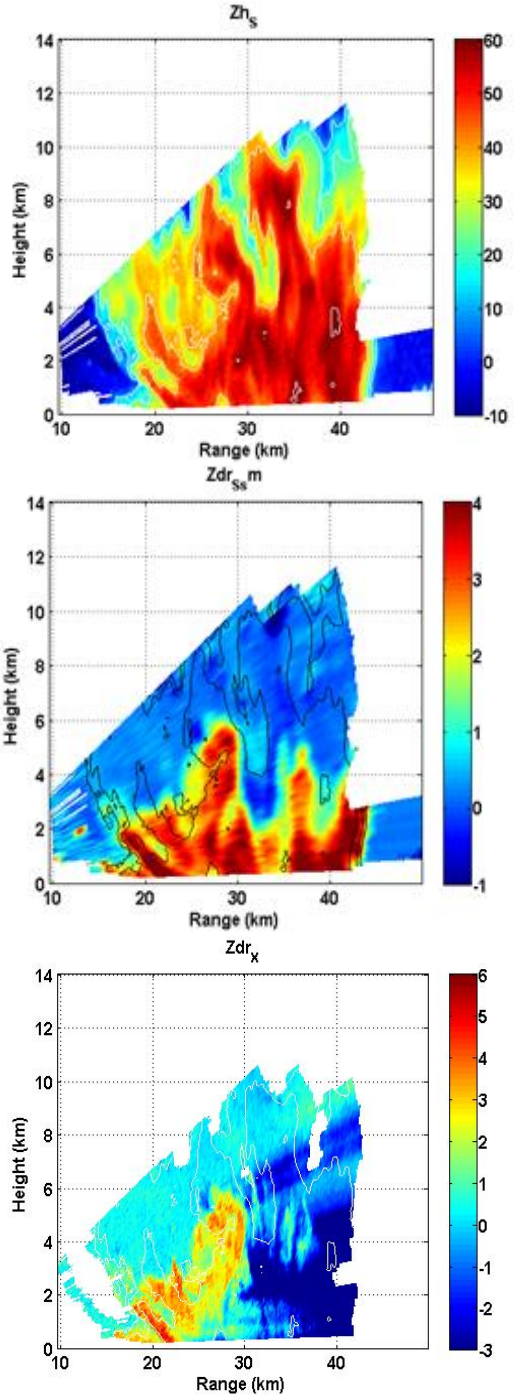

Fig. 8: CHILL RHI scans of S-band Z_h (top panel); S-band Z_{dr} (middle); X-band Z_{dr} (bottom panel) showing a 'wall' of negative Z_{dr} at X-band, at ~30 km range which may well be scattering effects, c.f. our model (A) results for the (relatively) larger-sized hail particles.

Fig. 9 shows extracted range profiles of S-band Z_h and the X-band Φ_{dp} (top panel) and the S and X band Z_{dr} (bottom panel). The sudden decrease in X band Z_{dr} can be seen at around 31 km range, this coinciding with high S-band reflectivity values and a noticeable component of X-band differential back-scatter phase. Using such information, together with our scattering calculations, inferences can be made about the sizes of melting hail particles causing such distinguishable features. This will be attempted in the future.

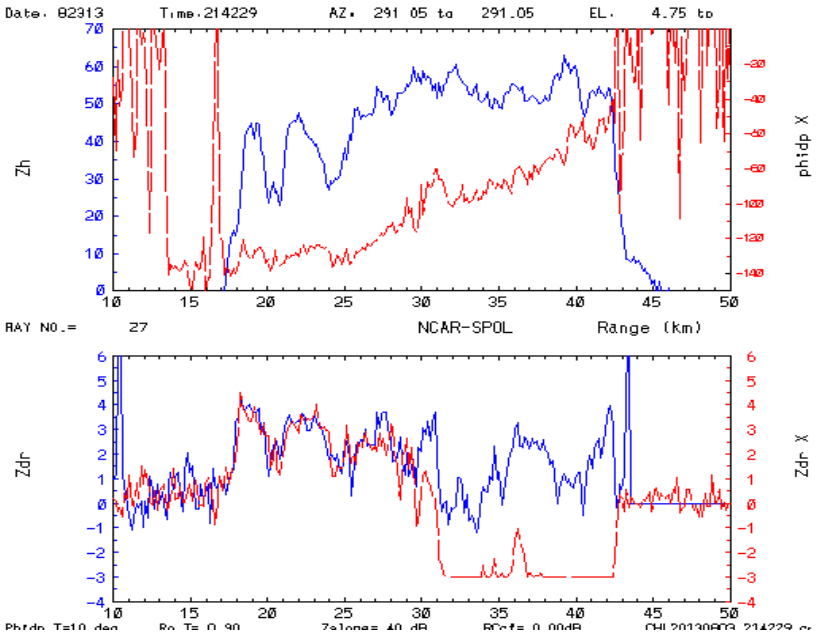

Fig.9: CHILL radar range profiles; see text for details. X-axis is range in km.

8 Summary

Our calculations using 2DVD based shape information of melting hail can explain unusually high Z_{dr} (from CHILL S-band radar observations) observed for one event which occurred over the 2DVD site. For another event, very negative Z_{dr} regions from an RHI scan from CHILL X-band radar observations can also be explained using our melting hail models.

Our calculations show that the polarimetric radar variables are quite sensitive to the shapes and sizes of melting hail particles. Hence, from the CHILL S and X band radar data for some particular events, it may be possible to make inferences on the melting hail particle characteristics using our model-based scattering calculations as a basis.

Acknowledgements

This work was supported by the National Science Foundation under grant AGS-1431127. Our thanks also to Pat Kennedy for the CHILL data and to Dr. Steve Rutledge for his interest, support and encouragement.

References

Bringi, V.N., and V. Chandrasekar, 2001: Polarimetric Doppler Weather Radar: Principles and Applications, Cambridge University Press, 636 pp.

CSU_CHILL radar: See Articles 2015 under http://www.chill.colostate.edu/

Djordjevic, M., Notaros, B. M., 'Double higher order method of moments for surface integral equation modeling of metallic and dielectric antennas and scatterers', IEEE Transactions on Antennas and Propagation, 2004, 52, (8), pp. 2118−2129,

Meischner, P. F., V. N. Bringi, D. Heimann, and H. Holler, 1991: A squall line in southern Germany: Kinematics and precipitation formation as deduced by advanced polarimetric and Doppler radar measurements. Mon. Wea. Rev., 119, 678–701

Rasmussen, R. M., Heymsfield, A. J., 1987: 'Melting and Shedding of Graupel and Hail. Part I', J. Atmos. Sci., 44, pp. 2754–2763.

Tabary, P., Vulpiani, G., Gourley, J. J., Illingworth, A. J., Thompson, R. J., Bousquet, O., 2009: 'Unusually High Differential Attenuation at C Band: Results from a Two-Year Analysis of the French Trappes Polarimetric Radar Data', J. Appl. Meteor. Climatol., 48, pp. 2037–2053

Thurai, M., G. J. Huang, V. N. Bringi, W. L. Randeu, and M. Schönhuber, 2007: Drop Shapes, Model Comparisons, and Calculations of Polarimetric Radar Parameters in Rain. J. Atmos. Oceanic Technol., 24, pp. 1019–1032.

Thurai, M., Chobanyan, E., Bringi, V. N., and Notaroš, B.M., 2015: Large Raindrops Against Melting Hail: Calculation of Specific Differential Attenuation, Phase and Reflectivity, Electronics Letters, 51, Issue 15, pp. 1140 –1142.